Highly-Compact Bearingless Axial-Flux Motor for a Pediatric Implantable Fontan Blood Pump

A. Horat [1], R. V. Giuffrida [1], S. Miric [2], M. Granegger [3], M. Hübler [4], J. Huber [1], J. W. Kolar [1]

[1] Power Electronic Systems Laboratory, ETH Zurich, Zurich, Switzerland
[2] Innsbruck Drive and Energy Systems Laboratory, University of Innsbruck, Innsbruck, Austria
[3] Department of Cardiac Surgery, Medical University of Vienna, Vienna, Austria
[4] Universitätsklinikum Hamburg-Eppendorf (UKE), Hamburg, Germany

Corresponding author: Andreas Horat, horat@lem.ee.ethz.ch
Speaker: Andreas Horat, horat@lem.ee.ethz.ch

Abstract

A pediatric implantable rotary blood pump (RBP) is under development in a research collaboration between the ETH Zurich, the University of Innsbruck, the University Medical Center Hamburg-Eppendorf and the Medical University of Vienna, in order to assist the Fontan circulation in newborns with a single ventricle. The RBP is driven by a small bearingless double-stator axial-flux permanent magnet synchronous machine, providing 2.2 mNm of torque at a rotational speed of 5500 rpm. The paper tackles the crucial challenge of defining an axial/angular position measurement concept with adequate resolution and bandwidth to enable magnetic levitation. As the sensors are integrated close the motor's winding, the measurement signals are significantly disturbed by stray fields generated by the phase currents. Such disturbances are compensated to obtain a usable signal for closed-loop position control. The experimental results show that, with the proposed compensation, the measurement errors are reduced to only 45 μm and 2.2°.

1   Introduction

One out of thousand children is born with a single ventricle [1], and the only treatment option is to undergo a series of three surgeries to create the Fontan circulation. Unfortunately, this is just a palliative solution and the patients' life quality and expectancy remains significantly limited. In fact, in the Fontan circulation, the single ventricle is responsible for sustaining both the systemic and pulmonary circulations, which are surgically connected in series through the total cavopulmonary connection (TCPC). This can lead to a progressive decline of the hemodynamics, ventricular failure, and even premature death [2]. These adverse consequences can be mitigated by using a cavopulmonary assist device (CPAD), i.e., an implantable blood pump. In the last decades, a large variety of rotary blood pumps (RBPs) has been developed and a few found its way to the clinical practice, but mainly for adult patients [3]. Only few VADs, mostly based on RBPs, meet the spatial requirements for long-term pedi-
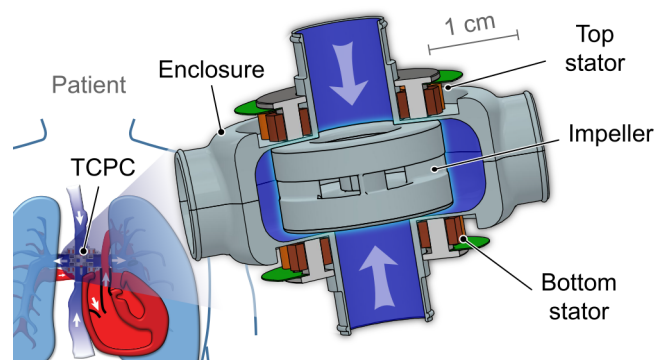
Fig. 1: The pediatric implantable cavopulmonary support device. The small blood pump is located at the total cavopulmonary connection (TCPC).

atric implantation, and could be re-purposed in the course of pilot studies [4]. In contrast, the development of (natively) pediatric implantable VADs has lagged behind, with the result that the only device approved is the Berlin EXCOR, a paracorporeal blood pump to support the left or right ventricle [5].

Recently, the company also introduced a cannula to support the cavopulmonary circulation of Fontan patients [6]. The *PediaFlow* [7], [8] and the *Jarvik 2015* [9] are two promising examples of natively pediatric VADs, where unfortunately only the first one is still under development. However, they are not tailored for cavopulmonary support in Fontan patients. Noticeably, a RBP based on a Bearingless Dual-Stator Axial-Flux Motor has been proposed [10], but it is not specifically designed for cavopulmonary support in Fontan patients, with a ≈ 30 % larger volume with respect to the proposed RBP. Furthermore, the chosen position sensors used to levitate the impeller are not integrated within the motor's volume. In this context, a long-term assistive cavopulmonary device, specifically designed to support the Fontan circulation, has been proposed in [11]. As illustrated in **Fig. 1(a)**, the small rotary blood pump is located at the TCPC, and propels the blood entering from its two axial inlets centrifugally to the two radial outlets. A first version of the pump with mechanical bearings has been designed, realized, and experimentally verified [11], [12]. The next step in the development is to exploit the key advantages of a magnetically levitated impeller, as in state-of-the-art third-generation rotary blood pumps [13]. This paper presents the electric motor required to drive the impeller and enable magnetic levitation, a Bearingless Dual-Stator Axial-Flux Motor (BDSAFM), i.e., with simultaneous bearing force and torque generation. Integrating magnetic bearings in the existing motor design is challenging. Of crucial importance is the choice of the appropriate displacement sensors, which is the focus of the paper. The sensors are required to measure and control the axial and angular positions of the impeller with sufficient accuracy and bandwidth. In particular, the number of sensors and their location in the system has to be defined properly, to guarantee satisfactory measurement accuracy. Furthermore, due to the targeted pediatric use, the device needs to be extremely compact, which significantly restricts the design options.

The paper is organized as follows. **Sec. II** describes the BDSAFM, explaining how torque and bearing force are generated. **Sec. III** discusses the position measurement concept with details on the sensors chosen, their location in the motor, and the required compensation of the measurement disturbances due to the phase currents in the winding. **Sec. IV** presents the realized motor prototype and

**Tab. 1:** Geometric parameters of the BDSAFM.

Name	Symbol	Value	Unit
Inner diameter	d_in	11.5	mm
Outer diameter	d_out	20.5	mm
Stator height	h_st	3.8	mm
Coil height	h_c	2.8	mm
PM thickness	d_PM	1.6	mm
Nominal air gap	d_ag	1.3	mm

the test bench needed to commission it. **Sec. V** reports the experimental measurements demonstrating successful correction of the measurement disturbances. Finally, **Sec. VI** concludes the paper.

2 Bearingless Dual-Stator Axial-Flux Motor

The proposed BDSAFM that drives and magnetically levitates the impeller is shown in **Fig. 2(a)**.

The chosen PMSM topology is based on the first version of the pump with mechanical bearings [11], [12]. The geometric parameters of the motor are reported in **Table 1**. Each of the two (top and bottom) stators has N_s = 9 slots and a multi-layer concentrated winding with N_c = 9 coils having N_t = 106 turns. Embedded in the impeller, there are two rotors, each interacting with one stator. Each rotor consists of a set of axially magnetized permanent magnets, creating N_p = 3 rotor pole pairs. Each set is backed by a thin disc of ferromagnetic material, which closes the magnetic circuit. Simultaneous torque and bearing force generation with the proposed BDSAFM can be explained considering the one-third sector view in **Fig. 1(b)**. Using field-oriented control with the electrical angle $\varphi_\text{el} = N_\text{p}\,\varphi_\text{mech}$, tangential force (and
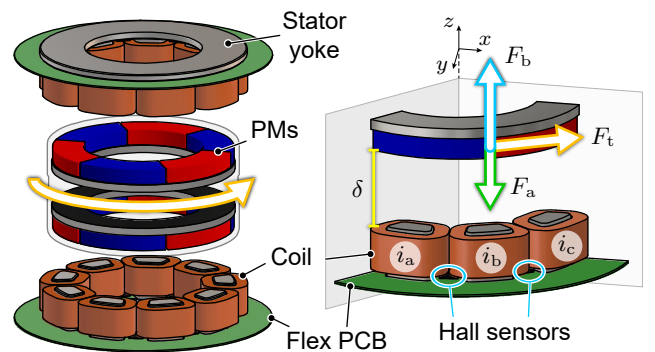
Fig. 2: The proposed bearingless, dual-stator, axial-flux motor (BDSAFM), together with a one-third section view to visualize its operating principle.

hence torque) generation is standard, i.e., it is obtained with the quadrature-component of the stator currents $i_{q,\{top,bot\}}$ in the rotor-oriented frame:

$$M_d = k_m \left(i_{q,top} + i_{q,bot} \right). \tag{1}$$

In a BDSAFM, the bearing force is instead generated by a combination of field weakening with one stator and field strengthening with the other, using the direct-component of the stator currents $i_{d,\{top,bot\}}$ in the rotor-oriented frame, hence

$$F_b = k_b \left(i_{d,top} - i_{d,bot} \right). \tag{2}$$

The generated bearing force F_b is controlled to counteract the magnetic attraction force F_a and maintain the rotor at the nominal distance $\delta_{\{top,bot\}}$ from the corresponding stator. F_a is the resultant of the reluctance forces existing between each rotor and its corresponding stator, and can be linearly approximated as

$$F_a = (F_{a,top} - F_{a,bot}) \approx k_a z_{sec}, \tag{3}$$

where $z_{sec} = \delta_{top} - \delta_{bot}$ thus defined is the axial position of the impeller (at the considered sector).

(a)

(b)
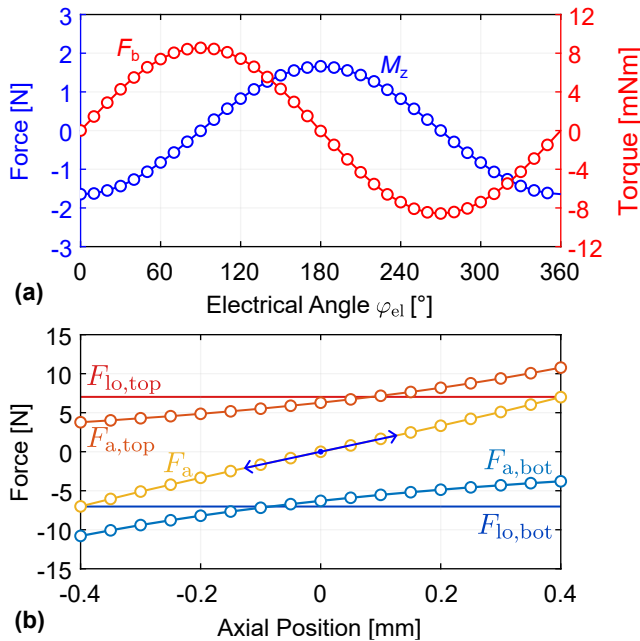
Fig. 3: (a) Simulated axial force and torque versus φ_{el} for 1 A of current amplitude. The peaks of the two curves are shifted by 90° electrical, indicating that force and torque generation are decoupled and correspond to the d- and q-components. **(b)** Simulated attraction forces for the top and bottom stators $F_{a,\{top,bot\}}$ and their difference, i.e. the net attraction force F_a, with a negative slope (stiffness).

This force has a destabilizing effect, as it points towards the stator with the smaller air gap length, and it would be zero only in the ideal condition of a perfectly axially centered impeller. Finally, to achieve full 6-DoF controllability of the impeller's position and orientation, i.e, including tilting about the x and y axes, at least three distinct bearing forces are required. Therefore, each sector needs to be controlled individually, which requires a total of 9 currents per stator, i.e., 18 phase currents for the full motor. The achievable torque and bearing machine constants are predicted using Finite Element Method (FEM) simulations. The results reported in **Fig. 3(a)** clearly show decoupled generation of the drive torque M_z and the bearing force F_b as indicated by **Eq. (1)** and **Eq. (2)**, with the machine constants $k_m = 8.6$ mN m/A and $k_b = 1.7$ N/A. Furthermore, an attraction constant (negative stiffness) of $k_a = 20$ N/mm is predicted (cf. **Fig. 3(b)**). Importantly, the simulated force at $z = \pm 0.4$ mm represents the liftoff force $F_{lo} = 8$ N that needs to be provided to the impeller at the startup.

3 Position Measurement Concept

To control the axial and angular positions of the impeller, accurate measurements are required. This section presents the proposed position measurement concept, with details on the chosen type of sensors, their number and location in the motor, and the compensation of the undesired measurement disturbances due to the phase currents.

3.1 Type/Number of Sensors and Post-Processing

Measuring the position of a sealed impeller requires contactless position sensors such as eddy-current or Hall sensors. Eddy-current sensors typically offer superior signal quality due to their high-frequency operating principle. [14] In contrast, Hall sensors are less robust against low frequency disturbances. Nevertheless, due to the extremely tight spatial constrains of the considered application, Hall sensors are selected. They are simple to use and available in miniature packaging formats, which allows for close integration within the volume of the motor. As illustrated schematically in **Fig. 4**, the proposed measurement concept requires six Hall sensors per sector, i.e., three per side, electrically displaced by 120° (corresponding to 40° mechanically with $N_p = 3$). This way, the measured magnetic flux densities $h_{\{1,2,3\}}$ and $h_{\{4,5,6\}}$ are ideally three 120°-phase-shifted sinusoidal signals for both top and bottom
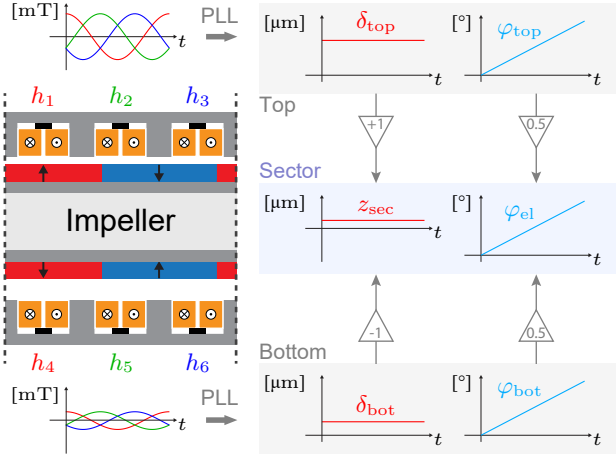
Fig. 4: Proposed measurement concept, requiring six Hall sensors per sector (three per side top/bottom). The measured flux densities are post-processed with PLLs to obtain an axial and angular position measurement per side $\delta_{\{\text{top,bot}\}}$ and $\varphi_{\{\text{top,bot}\}}$. The two are subtracted to obtain the axial position measurement of the sector z_{sec}, and averaged for φ_{el}.

sides. From these, two PLLs are used to provide two measurements of the angular position of the impeller $\varphi_{\{\text{top,bot}\}}$. The angle $\varphi_{\text{el}} = 0.5\,(\varphi_{\text{top}} + \varphi_{\text{bot}})$ is then used both for field-oriented control and to calculate the angular speed ω_z. The amplitude information returned by the PLLs is instead used to determine two measurements $\delta_{\{\text{top,bot}\}}$ of the axial position of the impeller. These are then subtracted to obtain the final differential measurement z_{sec} for each sector, finally used for magnetic levitation control.

3.2 Sensor Location and Sensitivity

In order to ensure that the signals $h_{\{1,\ldots,6\}}$ meet the desired ideal conditions as far as possible, the most favorable location of the sensors in the motor is studied using 3D FEM simulations. This is an essential step, as it guides the selection of an appropriate Hall sensor offering sufficient axial position sensitivity and bandwidth. Due to the tight spatial constraints in the considered stator geometry, there is very few options. The outer dimensions of a single sensor (including connecting pins) are limited to a maximum of 2-by-2 mm, in order to fit within a stator slot. It is only possible to place a thin flex-PCB hosting the Hall sensors either above the coils (top of the teeth, **Case 1**) or below the coils (bottom of the teeth, **Case 2**), as visible in **Fig. 5(a)**. Moreover, the total thickness of the sensor and the flex-PCB should be minimized as far as possible, to avoid reducing the height (i.e., number of turns) of
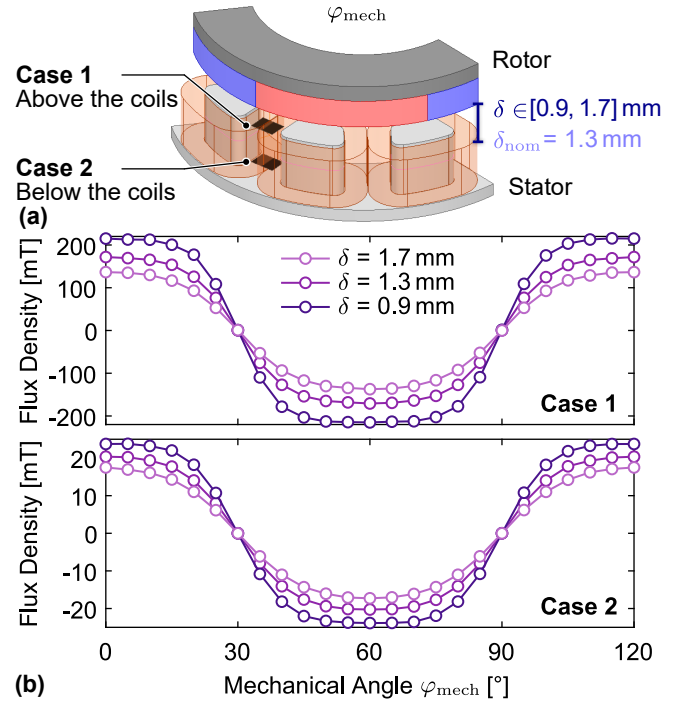
Fig. 5: **(a)** Sector view with two possible locations for the Hall sensors, i.e., above or below the coils. **(b)** Corresponding 3D-FEM results for the two considered locations and different values of the air gap δ. The signals exhibit a third harmonic distortion.

the coils excessively. The FEM results in **Fig. 5(b)** show the average magnetic flux density B_{hall}, calculated over the sensor planes indicated in **Fig. 5(a)**, versus the rotary position φ_{mech}. With a peak of 180 mT, the signal amplitude for **Case 1** is too large, with the risk of saturating the Hall element of the sensor, especially for the case $\delta_{\text{min}} = 0.9$ mm (z_{sec} = –0.4 mm, touchdown). An off-the-shelf sensor of suitable dimensions with such measurement range could in fact not be found. Therefore, as already visible in **Fig. 2**, the selected location is at the bottom of the stator's teeth, i.e., **Case 2**. With an amplitude of 17.5 mT at $\delta_{\text{max}} = 1.7$ mm (furthest), 20 mT at $\delta_{\text{nom}} = d_{\text{ag}} = 1.3$ mm (nominal), and 24 mT at δ_{min} = 0.9 mm (closest), the predicted axial position sensitivity is of about 8.1 mT/mm. The chosen sensor is the *ams AS5510*, which offers a resolution of 97 µT and a sampling frequency of 20 kHz. Therefore, the achievable axial position resolution is of 12 µm, which is adequately small compared to the considered 0.8 mm range of axial motion. Noticeably, for both cases there is a certain (spatial) third harmonic distortion on the measured flux density. As visible further in **Fig. 8**, this translates into a tolerable magnitude ripple of 50 µm.

## 3.3 Measurement Disturbance due to the Phase Currents

A crucial problem to consider is that, by being placed very closely to the motor's winding, the Hall sensors are inevitably disturbed by the phase currents. The entity of such disturbance can be studied in detail with the aid of FEM simulations. To first visualize and describe it qualitatively, consider the magnetic field distribution in **Fig. 6**, obtained with FEM simulations for a simplified 2D geometry. To solely include the magnetic field generated by the currents circulating in the coils, the PMs are removed from the model at this stage. It is hence assumed that the field component generated by the phase currents and the one generated by the PMs can be superimposed, and that the relative permeability of the PMs is $\mu_{\mathrm{r,PM}} \approx \mu_0$. For this analysis, an ideal ferromagnetic linear material ($\mu_{\mathrm{r,Fe}}$ = 4000) is chosen for the magnetic cores. Consider now the chosen sensor location at the bottom of a stator slot. When the two adjacent coils are energized, in this example with the same current $I_{\mathrm{left}} = I_{\mathrm{right}} = I_{\mathrm{test}} = 1\,\mathrm{A}$, there is some stray field through the sensor at the selected sensor location. With an average value of 20 mT, this disturbance is as large as the measurement signal. Therefore, it is necessary to consider it explicitly, characterize it in detail, and finally compensate it. It is also a further reason to place the Hall sensors away from the rotor, as the current disturbance could potentially saturate the sensors.

3.3.1 Characterization on a Single Sensor

The detailed characterization of the disturbance introduced by the phase currents is conducted on the complete 3D FEM model of the motor (i.e., with nonlinear materials and PMs included). The
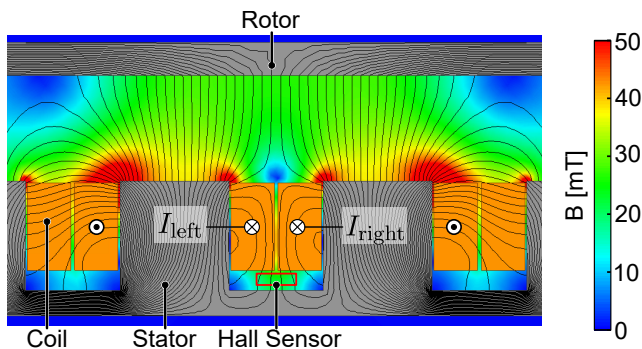
Fig. 6: Simplified 2D-FEM simulation to visualize the magnetic field distribution generated by the currents in the coils, causing a stray field that disturbs the sensor's measurement signal.
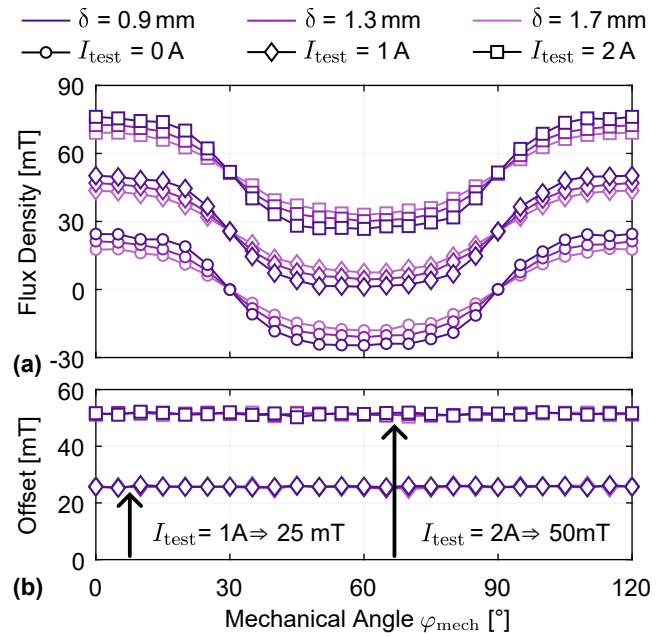
Fig. 7: FEM characterization of the measurement disturbance on a single sensor. **(a)** Average flux densities at the sensor plane for different axial positions and currents. **(b)** Calculated offsets for the cases I_{test} = 1 A and 2 A by subtracting the corresponding values obtained for I_{test} = 0 A. The offset scales linearly with current and does nearly not depend on the rotor's axial/angular position.

goal is to assess whether the amount of stray field through the sensor depends on the axial and angular positions of the rotor, and to verify its linearity with respect to the assigned current excitation in the adjacent coils. Therefore, the simulations are conducted for different angular and axial positions (again φ_{mech} = {0,5,...120}° and δ = {0.9,1.3,1.7} mm) and currents (I_{test} = {0,1,2}A, with the same current I_{test} in the two adjacent coils), obtaining the results of **Fig. 7(a)**. As can be observed, the flux density curves are the same as in **Case 2** of **Fig. 5(b)** for I_{test} = 0 A, and they are shifted up by a certain offset for the other two cases I_{test} = {1,2}A. This can be better visualized in **Fig. 7(b)**, showing the difference between the signals for I_{test} = {1,2}A and the corresponding ones for I_{test} = 0 A. With an offset of 25 mT for I_{test} = 1 A and 50 mT for I_{test} = 2 A, the linearity of the disturbance is verified, with 25 mT/A. Furthermore and importantly, the disturbance offset does not exhibit any relevant dependency on the axial or angular positions of the rotor. This result is reasonable and can be understood by observing how the stray field closes within the stator itself in **Fig. 6**.
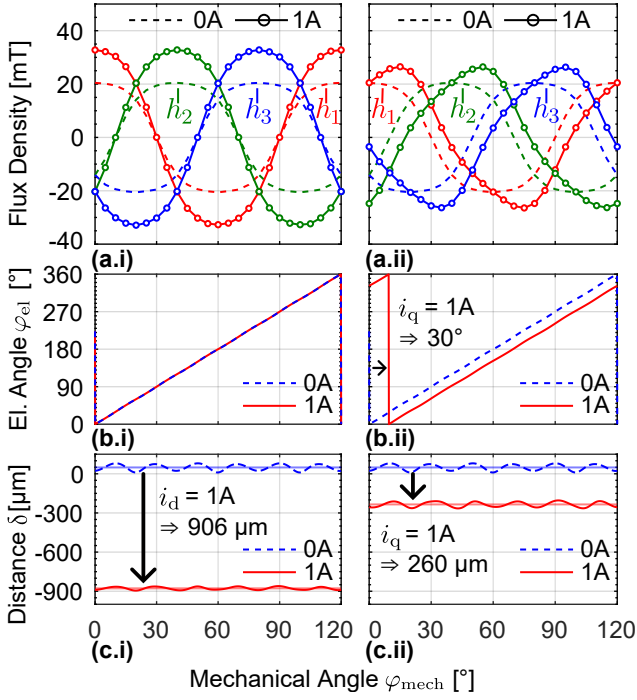
Fig. 8: FEM characterization of the measurement disturbance for typical operation with **(.i)** $i_d = 1$ A and **(.ii)** $i_q = 1$ A. **(a)** Average flux densities $h_{\{1,2,3\}}$ at the three sensor planes of a sector side (top or bottom). **(b)** Calculated angle using the PLL. **(c)** Calculated amplitude using the PLL.

3.3.2 Characterization for Typical Operation

With these intermediate simulation results, the analysis can be brought a step further. Assigning the same current to both the adjacent coils is useful to study and characterize the disturbance on a single sensor, but is a case that never occurs in practice. Two realistic cases for typical operation are when d- and q-currents are assigned to the motor's winding for field-oriented control. As seen, the former is used to generate the bearing force, whereas the latter for the drive torque. For the FEM results of **Fig. 8**, the nominal axial position $\delta = 1.3$ mm ($z_{\text{sec}} = 0$ mm) and 1 A of d- or q-current are considered. The analysis is extended to one side of a sector, i.e., considering three sensor signals $h_{\{1,2,3\}}$. For the d-case, $h_{\{1,2,3\}}$ are amplified by a factor 1.6, which is due to field strengthening. This does not influence the electrical angle φ_{el} detected by the PLL, but of course strongly influences the amplitude and hence the detected axial position δ, with a large error of 906 μm. Conversely, for the q-case, the signals $h_{\{1,2,3\}}$ are rather distorted. This affects both the detected electrical angle φ_{el}, with about 30° of error, and the amplitude δ, with a less pronounced but still relevant 260 μm error. Therefore,
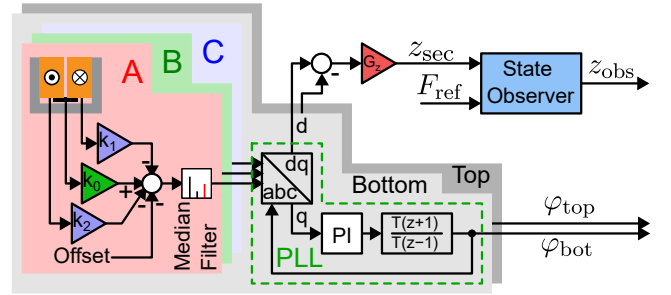
Fig. 9: Diagram of the post-processing of the Hall signals, with the proposed disturbance compensation (one sector).

as expected, it is essential to compensate the studied disturbance, i.e. to derive a signal suitable for controlling the impeller's position.

3.4 Proposed Disturbance Compensation

The complete diagram of the Hall sensor signals post-processing is shown in **Fig. 9**. The disturbance due to the phase currents is compensated individually for each sensor before feeding the signals to the PLLs. This is because, in practice, the manufacturing tolerances will influence the final position of each sensor in the motor. Due to the verified linearity, the disturbance can be modeled by a simple weighted sum and can be compensated as

$$h_{\text{comp}} = k_0 \cdot h_{\text{raw}} - \hat{k}_1 \cdot I_1 - \hat{k}_2 \cdot I_2, \qquad (4)$$

where $k_0 \approx 1$ is an adjustment factor to account for sensor and manufacturing tolerances. The estimated factors $\hat{k}_1$ and $\hat{k}_2$ depend on the exact coil geometry and sensor position and should hence be specifically calibrated. As explained further in **Sec. 5.1**, due to the limited sampling frequency of the Hall sensor and its inherent transmission delay, a median filter is used to further improve the signals when an incorrect compensation occurs. The further processing of the compensated signals is straightforward and follows the same steps already illustrated in **Fig. 4**.

4 Hardware Prototype and Test Bench

The hardware prototype of the BDSAFM is shown in **Fig. 10**. The stator yoke and the rotor back iron are realized with special ferromagnetic materials, namely the *Valbruna MG2* and the *VACOFLUX50*, which offer high magnetic saturation (2 T and 2.3 T), and are hence particularly suited for a compact realization. The nine concentrated coils have $N_t =$

106 turns and are realized with a 0.125 G1B enameled copper wire. Finally, the permanent magnets are custom made with thickness $d_{\mathrm{PM}} =$ 1.6 mm and N48 magnetization grade. The motor is fed by a custom 18-phase inverter, based on the *MP6536* (*Monolithic Power Supply*) three-phase inverter module. The controller is implemented on a *AMD Xilinx Zynq 7020* module. Due to the number of current controllers to be executed simultaneously, they are implemented in the FPGA. They are executed with an update rate of 500 kHz allowing a bandwidth of $f_{\mathrm{cc}} =$ 10 kHz. To commission the proposed BDSAFM, the test bench in **Fig. 10** is realized. The impeller assembly (containing the two rotors) is connected to a 6-axis force/torque sensor (*BOTA systems*) mounted to a top fixture. This allows measuring not only the generated torque, the axial attraction force, and the bearing force, but also the tilting torques applied to the impeller. This can be done for different relative positions of the impeller and the stator assembly, which is mounted on two precision vertical (*standa 7VT174-5*) and rotary (*standa 7R150*) positioning stages, fixed to the baseplate. The stator assembly features an interconnection PCB and a round stainless steel mount replacing the pump's enclosure.

5 Experimental Results

This section presents the experimental measurements conducted on the presented testbench. These include the verification of the machine constants and of the measured sensor signals, with
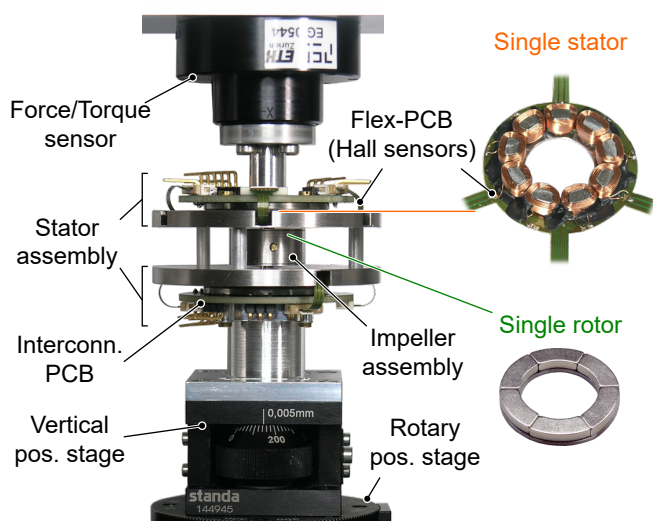
Fig. 10: Experimental test bench for the proposed BD-SAFM. The stator and rotor assemblies are shown in detail.

particular focus on the proposed disturbance compensation.

5.1 Machine Constants and Sensor Signals Verification

The measurements in **Fig. 11(a)** demonstrate successful and well-decoupled torque and bearing force generation, with the torque constant $k_{\mathrm{m}} =$ 9.1 mN m/A and the bearing constant $k_{\mathrm{b}} =$ 1.6 N/A per stator (top and bottom). The measured attraction constant is $k_a =$ 15 N/mm. With the maximum z-position of $z_{\max} =$ 0.4 mm, it results to a maximum required liftoff force of $F_{\mathrm{lo}} =$ 6.0 N. The required liftoff current is hence $i_{\mathrm{d,lo}} =$ 1.88 A. Finally, the measured Hall sensor signals are shown in **Fig. 11(b)**. The signal amplitude of 25 mT corresponds to the predicted one from FEM, and also the expected third harmonic distortion is visible.

5.2 Disturbance Compensation: Calibration

The individual position of each sensor introduces a gain factor, which is measured by normalizing the sensor amplitude when rotating the mover at a fixed vertical and radial position. It is crucial that the impeller is centered vertically, such that the difference of the amplitudes is zero. The sensor zero value offset is specified as maximum 0.45 mT, translating to
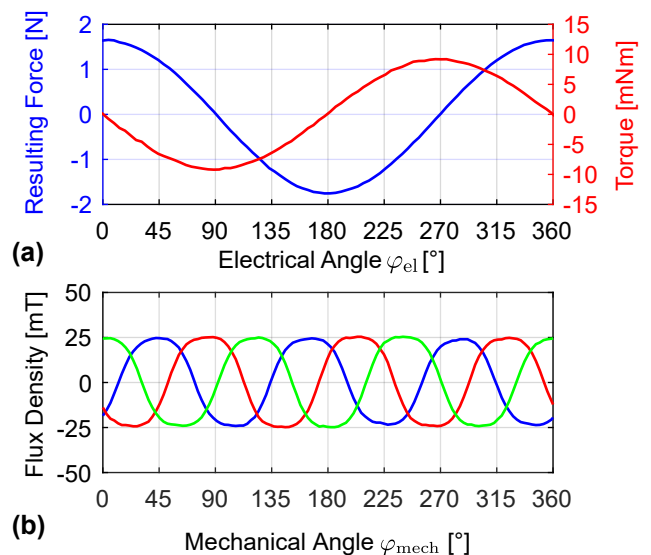
Fig. 11: (a) Measured force and torque generated for a fixed, horizontal rotor position and a rotating stator field with $\hat{I} =$ 1 A. The torque- and bearing force-generating components are clearly decoupled. **(b)** Measured sensor signals of a sector side for a complete revolution of the impeller at the nominal (centered) axial position.

a maximum offset of 30 bit. This offset is measured without a rotor present and zero phase currents and then subtracted from the measured signal. The disturbance compensation factors ($\hat{k}_1$ and $\hat{k}_2$, for each sensor) are calibrated at the nominal (centered) axial position $z = 0\,\mu m$ with the rotor mechanically fixed and positioned using the test bench. To determine the individual compensation factors for each sensor, the electrical angle is assigned such that only one of the two adjacent coils at a time carries a current. As it is not possible to thermally sustain a continuous DC current in the winding for the whole duration of the measurements, it is decided to apply four short (20 ms duration) current steps with amplitudes from 0.5 A to 2 A in steps of 0.5 A. As shown in **Fig. 12** (red signal – uncompensated), the linearity of the disturbance is verified, at least at the considered axial position, with 10 mT/A. However, for the 2 A case, a slight saturation of the rotor core leads to an overcompensation. All in all, the proposed compensation proves to be effective for currents till about 1.5 A and low frequency, with a maximum residual signal disturbance of only 2 mT. Importantly, the magnified signal edge shows that the compensation results incorrect for the first two samples after a current step. This is due to the


(a)

(b)
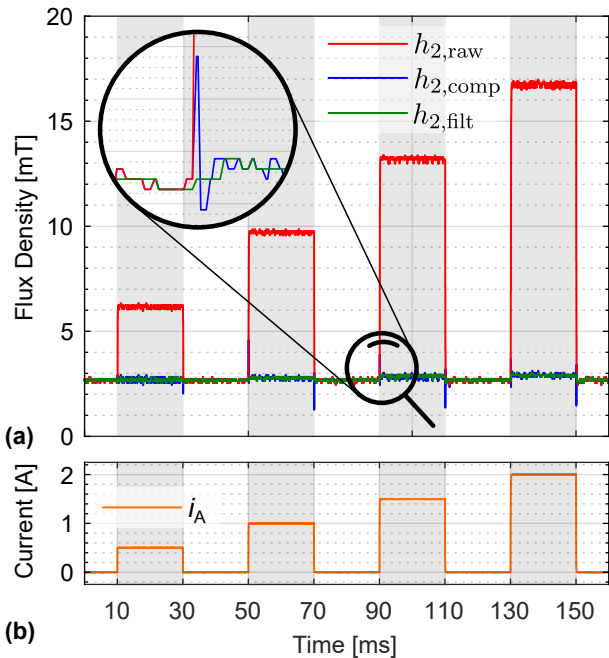
Fig. 12: Investigation of the measurement disturbance on a single sensor without and with compensation. The zoomed view shows the effectiveness of the median filter in suppressing the signal spikes occurring due to incorrect compensation at the edge of the current steps.

low possible readout frequency of the Hall sensor, i.e. 20 kS/s, compared with the high current sampling rate of 500 kHz and controller bandwidth of 10 kHz. For the chosen Hall sensor, the frequency behavior is not entirely specified, and it is hence investigated experimentally. No low pass behavior could be observed up to 2 kHz. However, the sensor exhibits a zero-order hold characteristic with 50 μs hold time. This can only be compensated accurately if the sampling frequency is well above the signal bandwidth or the sampling instant is exactly known. Neither is the case for fast-changing current steps with a current controller bandwidth of 10 kHz. This leads to an over- or under-compensation for one to two measurement samples. These disturbances are estimated to be above 100 μm, which is not acceptable for magnetic levitation. For this reason, a median filter with window three is used to successfully suppress the uncompensated spikes with minimal additional phase lag.

5.3 Disturbance-Compensated Measurements for Typical Operation

Once the compensation factors for each sensor are calibrated, the effectiveness of the proposed compensation for the realistic case of d- and q-current excitations can be assessed experimentally. Also in this case the rotor is fixed in the test bench and its position adjusted with the positioning stages. Two short d- and q-current steps are commanded. The amplitude of the d-current step is inverted to −1 A, to emulate the current step necessary for liftoff in the bottom stator. The measurements are conducted for three axial positions ($z = \{-0.4, 0, 0.4\}$mm) and three angular positions ($\varphi_{\text{el}} = \{0, 30, 60\}\,°$). An exemplary repetition is reported in **Fig. 13**. The three Hall sensors of one sector are recorded (cf. **Fig. 13 (a)**) and used to derive the axial and rotational positions. The d-current step leads to an axial position error of 600 μm, whereas the rotational angle is only disturbed marginally, with an error of about 2°. Also in this case, if uncompensated, the disturbance in the axial position is larger than the axial motion range. The disturbance on the rotational angle is non-zero due to machine imperfections. For the q-current step, the expected angle error of 24° can be measured, as well as an error in the axial position measurement of 200 μm. The proposed compensation reduces the influence of the stray magnetic field created by the phase currents by a factor of about 10 to a value below ±45 μm.
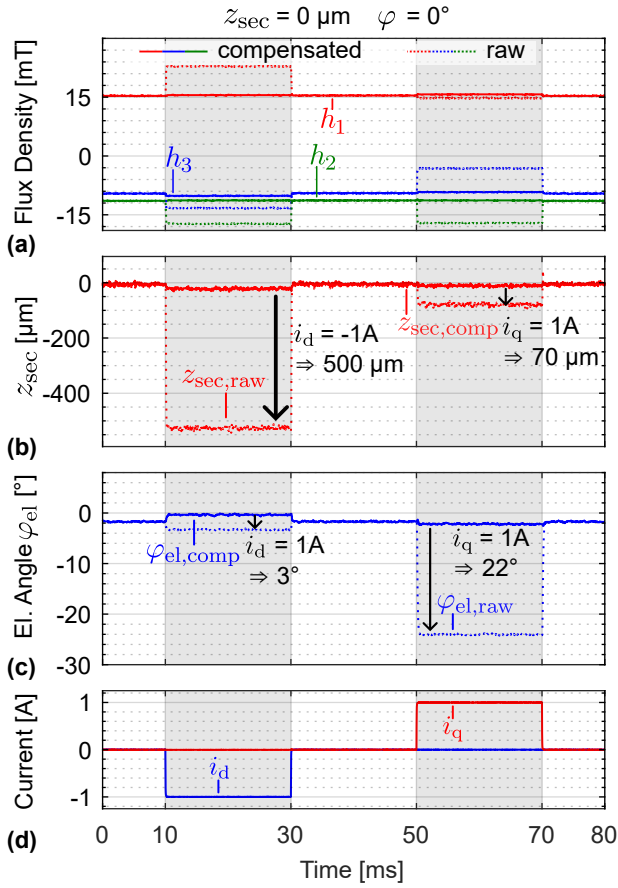
Fig. 13: Final measurement of the calculated z_{sec} and φ_{el} in one sector shown as measured (raw) values and with the proposed compensation over time. **(a)** Flux density $h_{1,2,3}$ of the three sensors. **(b)** measured z_{sec} disturbance. **(c)** electrical angular disturbance φ_{el}. **(d)** current pulses in d- and q-axis.

z_{sec}	$-0.4\,\mathrm{mm}$		$0\,\mathrm{mm}$		$0.4\,\mathrm{mm}$	
φ_{el}	i_d	i_q	i_d	i_q	i_d	i_q
$0°$	14.4	14.0	23.9	31.7	45.0	18.0
$30°$	17.0	6.9	29.6	33.2	39.2	14.2
$60°$	18.1	8.1	33.7	25.0	42.2	10.9

Tab. 2: Maximum absolute z-position error in micrometer for all six sectors at maximum and minimum height and three electrical angles when disturbed with $i_d = -1\,\mathrm{A}$ or $i_q = 1\,\mathrm{A}$.

z_{sec}	$-0.4\,\mathrm{mm}$		$0\,\mathrm{mm}$		$0.4\,\mathrm{mm}$	
φ_{el}	i_d	i_q	i_d	i_q	i_d	i_q
$0°$	1.53	0.58	1.33	1.44	2.02	1.89
$30°$	1.46	1.17	1.19	0.62	1.97	0.78
$60°$	1.90	2.03	1.47	1.35	1.76	0.27

Tab. 3: Maximum absolute angular position error in degrees for all six sectors at maximum and minimum height and three electrical angles when disturbed with $i_d = -1\,\mathrm{A}$ or $i_q = 1\,\mathrm{A}$.

6 Conclusion

Pediatric implantable rotary blood pumps (RBPs), specifically designed for cavopulmonary support in Fontan circulation and currently under development in a research collaboration between ETH Zürich, the University of Innsbruck, the University Medical Center Hamburg-Eppendorf and the Medical University of Vienna shall exploit the key advantages of magnetic bearings for improved durability and hemocompatibility. However, the design and integration of extremely compact bearingless motors poses numerous challenges, especially for the position measurement of the levitated impeller. In this paper, an axial/angular position measurement concept for a compact bearingless double-stator axial-flux motor (BLDSAFM) has been proposed. Importantly, this requires a compensation of the measurement disturbances caused by the currents in the motor windings. The experimental results demonstrate that the compensation works and that clean and usable position measurement signals with disturbances below 45 µm and 2.2° can be achieved. Therefore, in future work, the proposed sensing concept can be used for closed-loop position control of the BLDSAFM.

References

[1] P. W. O'Leary, "Prevalence, Clinical Presentation and Natural History of Patients with Single Ventricle," *Progress in Pediatric Cardiology*, vol. 16, no. 1, pp. 31–38, 2002.

[2] M. Gewillig, "The Fontan Circulation," *Heart*, vol. 91, no. 6, pp. 839–846, 2005. DOI: 10.1136/HRT.2004.051789.

[3] S. M. Moisă, A. Burlacu, C. Brinza, E. Cinteză, L. I. Butnariu, *et al.*, "An Up-to-Date Literature Review on Ventricular Assist Devices Experience in Pediatric Hearts," *Life*, vol. 12, no. 12, 2022. DOI: 10.3390/life12122001.

[4] I. Adachi, S. Burki, and C. D. Fraser, "Current Status of Pediatric Ventricular Assist Device Support," *Seminars in Thoracic and Cardiovascular Surgery: Pediatric Cardiac Surgery Annual*, vol. 20, pp. 2–8, 2017. DOI: 10.1053/j.pcsu.2016.09.010.

[5] C. S. Almond, D. L. Morales, E. H. Blackstone, M. W. Turrentine, M. Imamura, *et al.*, "Berlin Heart EXCOR Pediatric Ventricular Assist Device for Bridge to Heart Transplantation in US Children," *Circulation*, vol. 127, no. 16, pp. 1702–1711, 2013. DOI: 10.1161/CIRCULATIONAHA.112.000685.

[6] B. Karner, E. Urganci, J. Schlein, E. Base, S. Greil, *et al.*, "First-in-man use of the EXCOR Venous Cannula for Combined Cavopulmonary and Systemic Ventricular Support in Fontan Circulation Failure," *The Journal of Heart and Lung Transplantation*, vol. 41, no. 10, pp. 1533–1536, 2022. DOI: 10.1016/j.healun.2022.06.009.

[7] H. S. Borovetz, S. E. Olia, and J. F. Antaki, "Toward the Development of the PediaFlow™ Pediatric Ventricular Assist Device: Past, Present, Future," *Applications in Engineering Science*, vol. 11, pp. 100–113, 2022. DOI: 10.1016/j.apples.2022.100113.

[8] M. D. Noh, J. F. Antaki, M. Ricci, J. Gardiner, D. Paden, *et al.*, "Magnetic Design for the PediaFlow Ventricular Assist Device," *Artificial Organs*, vol. 32, no. 2, pp. 127–135, 2008. DOI: 10.1111/j.1525-1594.2007.00501.x.

[9] I. Adachi, S. Burki, F. Zafar, and D. L. S. Morales, "Pediatric Ventricular Assist Devices," *Journal of Thoracic Disease*, vol. 7, no. 12, pp. 2194–2202, 2015. DOI: 10.3978/j.issn.2072-1439.2015.12.61.

[10] M. Osa, T. Masuzawa, K. Yamaguchi, and E. Tatsumi, "Double Stator Axial Gap Type Ultra-Compact 5-DOF Controlled Self-Bearing Motor for Rotary Pediatric Ventricular Assist Device," *IEEE Transactions on Industry Applications*, vol. 57, no. 6, pp. 6744–6753, 2021.

[11] A. Escher, C. Strauch, E. J. Hubmann, M. Hübler, D. Bortis, *et al.*, "A Cavopulmonary Assist Device for Long-Term Therapy of Fontan Patients," in *Seminars in Thoracic and Cardiovascular Surgery*, Elsevier, vol. 34, 2022, pp. 238–248.

[12] E. J. Hubmann, D. Bortis, M. Flankl, J. W. Kolar, M. Granegger, *et al.*, "Optimization and Calorimetric Analysis of Axial Flux Permanent Magnet Motor for Implantable Blood Pump Assisting the Fontan Circulation," in *Proc. of the IEEE 22nd Intern. Conf. on Electr. Machines and Systems (ICEMS)*, IEEE, 2019, pp. 1–8.

[13] H. Hoshi, T. Shinshi, and S. Takatani, "Third-Generation Blood Pumps with Mechanical Non-contact Magnetic Bearings," *Artificial Organs*, vol. 30, no. 5, pp. 324–338, 2006.

[14] A. J. Fleming, "A review of nanometer resolution position sensors: Operation and performance," *Sensors and Actuators A: Physical*, vol. 190, pp. 106–126, 2013. DOI: 10.1016/j.sna.2012.10.016.